

A hot terrestrial planet orbiting the bright M dwarf L 168-9 unveiled by TESS *,**,***

N. Astudillo-Defru¹, R. Cloutier²,³, S. X. Wang⁴, J. Teske⁴,****, R. Brahm^{5,6,7}, C. Hellier⁸, G. Ricker⁹, R. Vanderspek⁹, D. Latham², S. Seager¹⁰, J. N. Winn¹¹, J. M. Jenkins¹², K. A. Collins², K. G. Stassun¹³, C. Ziegler¹⁴, J. M. Almenara¹⁵, D. R. Anderson^{8,16}, E. Artigau¹⁷, X. Bonfils¹⁵, F. Bouchy¹⁸, C. Briceño¹⁹, R. P. Butler²⁰, D. Charbonneau², D. M. Conti²¹, J. Crane⁴, I. J. M. Crossfield^{22,23}, M. Davies¹², X. Delfosse¹⁵, R. F. Díaz^{24,25}, R. Doyon¹⁷, D. Dragomir²⁶, J. D. Eastman², N. Espinoza²⁷, Z. Essack¹⁰, F. Feng²⁰, P. Figueira^{28,41}, T. Forveille¹⁵, T. Gan³⁰, A. Glidden⁹, N. Guerrero⁹, R. Hart³¹, Th. Henning³², E. P. Horch³³, G. Isopi³⁴, J. S. Jenkins³⁵, A. Jordán^{36,7}, J. F. Kielkopf³⁷, N. Law³⁸, C. Lovis¹⁸, F. Mallia³⁴, A. W. Mann³⁸, J. R. de Medeiros³⁹, C. Melo²⁸, R. E. Mennickent²⁹, L. Mignon¹⁵, F. Murgas¹⁵, D. A. Nusdeo⁴⁰, F. Pepe¹⁸, H. M. Relles², M. Rose¹², N. C. Santos^{41,42}, D. Ségransan¹⁸, S. Shectman⁴, A. Shporer⁹, J. C. Smith^{43,12}, P. Torres⁵, S. Udry¹⁸, J. Villasenor⁴⁴, J. G. Winters², and G. Zhou²

(Affiliations can be found after the references)

Received 22 November 2019 / Accepted 27 January 2020

ABSTRACT

We report the detection of a transiting super-Earth-sized planet $(R = 1.39 \pm 0.09 \ R_{\oplus})$ in a 1.4-day orbit around L 168-9 (TOI-134), a bright M1V dwarf (V = 11, K = 7.1) located at 25.15 ± 0.02 pc. The host star was observed in the first sector of the Transiting Exoplanet Survey Satellite (TESS) mission. For confirmation and planet mass measurement purposes, this was followed up with ground-based photometry, seeing-limited and high-resolution imaging, and precise radial velocity (PRV) observations using the HARPS and Magellan/PFS spectrographs. By combining the TESS data and PRV observations, we find the mass of L 168-9 b to be $4.60 \pm 0.56 \ M_{\oplus}$ and thus the bulk density to be $1.74^{+0.44}_{-0.33}$ times higher than that of the Earth. The orbital eccentricity is smaller than 0.21 (95% confidence). This planet is a level one candidate for the TESS mission's scientific objective of measuring the masses of 50 small planets, and it is one of the most observationally accessible terrestrial planets for future atmospheric characterization.

Key words. stars: individual: L 168-9 – planetary systems – stars: late-type – techniques: photometric – techniques: radial velocities

1. Introduction

Transiting planets are the best planet candidates for performing detailed characterizations, first and foremost, because they allow for the possibility of unambiguous mass measurements (e.g., HD 209458b, Charbonneau et al. 2000; Mazeh et al. 2000; Henry et al. 2000). We can determine the minimum mass of the planet $(m \sin i)$ from the Doppler effect and also the planetary radius and the orbital inclination (i) from the transit light curve, thus yielding a measurement of the planet's mass. Moreover, from this combination, we can calculate the planet's mean density and shed light on its internal structure by comparing it with models containing different amount of iron, silicates, water, hydrogen, and helium. Furthermore, transiting planets are unique because of the feasibility in characterizing the upper atmosphere by spectroscopy during transits and occultations of a significant number of planets. The forthcoming James Webb Space Telescope (JWST, Gardner et al. 2006) and the Extremely Large

Telescope (ELT, de Zeeuw et al. 2014) will have unprecedented capabilities in performing detailed studies of the atmospheres of terrestrial planets, and the interpretation of the results will require an accurate mass measurement (e.g., Batalha et al. 2019).

Scientific operations in the Transiting Exoplanet Survey Satellite (TESS; Ricker et al. 2015) started in July 2018; the aim of which is to detect transiting planets around bright and nearby stars that are bright enough for Doppler mass measurements. For this task, TESS surveys about 85% of the sky during the prime mission. The survey covering the southern ecliptic hemisphere is now complete, and the northern survey is underway. Each hemisphere is divided into 13 rectangular sectors of $96^{\circ} \times 24^{\circ}$ each. Each sector is continuously observed for an interval of 27-days, with a cadence of 2 min for several hundreds of thousands of preselected stars deemed best suited for planet searching. Additionally, during the TESS prime mission, the full frame images, which consist of the full set of all science and collateral pixels across all CCDs of a given camera, are available with a cadence of 30 min. M dwarfs are of special interest because the transit and radial-velocity signals of a given type of planet are larger for these low-mass stars than they are for Sun-like stars. In addition, compared to hotter stars, M dwarfs present better conditions for the detection of planets orbiting the circumstellar habitable zone: performing surveys in M dwarfs is less time consuming, and there are larger Doppler signals and an increased transit probability. Sullivan et al. (2015) anticipates that out of the 556

^{*} Full Tables B.1 and B.2 are only available at the CDS via anonymous ftp to cdsarc.u-strasbg.fr (130.79.128.5) or via http://cdsarc.u-strasbg.fr/viz-bin/cat/J/A+A/636/A58.

^{**} Partially based on observations made with the HARPS instrument on the ESO 3.6 m telescope under the program IDs 198.C-0838(A), 0101.C-0510(C), and 1102.C-0339(A) at Cerro La Silla (Chile).

^{***} This paper includes data gathered with the 6.5 m *Magellan* Telescopes located at Las Campanas Observatory, Chile.

^{****} NASA Hubble Fellow.

small ($<2 R_{\oplus}$) transiting planets discovered by TESS, 23% of them will be detected orbiting bright ($K_S < 9$) stars and that 75% of small planets will be found around M dwarfs.

This paper reports the discovery of a small planet orbiting the star L 168-9 (TOI-134), based on TESS data. The host star is a bright M dwarf. An intense precise radial-velocity campaign with HARPS and the Planet Finder Spectrograph (PFS) has revealed the terrestrial nature of the newly detected world. This work is presented as follows: Sect. 2 describes the host star properties. Sections 3.1 and 3.3 describe the photometric and radial-velocity observations. Section 4 presents an analysis of all the data, including the study of stellar activity. Finally, Sect. 6 places L 168-9 b within the larger context of the sample of detected planets.

2. L 168-9

L 168-9, also known as CD-60 8051, HIP 115211, 2MASS J23200751-6003545, with the entry 234994474 of the TESS input catalog (TIC) or 134 of the TESS object of interest (TOI) list, is a red dwarf of spectral type M1V. It appears in the southern sky and resides at a distance of 25.150 ± 0.024 pc from the Sun (Gaidos et al. 2014; Gaia Collaboration 2018). Table 1 lists the key parameters of the star, namely its position, visual and near-infrared apparent magnitudes, parallax, proper motion, secular acceleration, and its essential physical properties.

We performed an analysis of the broadband spectral energy distribution (SED) together with the *Gaia* DR2 parallax in order to determine an empirical measurement of the stellar radius, following the procedures described by Stassun & Torres (2016) and Stassun et al. (2017, 2018a). We took the B_TV_T magnitudes from *Tycho*-2, the *BVgri* magnitudes from APASS, the *JHK_S* magnitudes from 2MASS, the W1–W4 magnitudes from WISE, and the *G* magnitude from *Gaia*. Together, the available photometry spans the full stellar SED over the wavelength range of 0.35–22 μ m (see Fig. 1).

We performed a fit using NextGen stellar atmosphere models (Hauschildt et al. 1999); the effective temperature ($T_{\rm eff}$) and surface gravity ($\log g$) were constrained on the ranges reported in the TIC (Stassun et al. 2018b), while the metallicity [Fe/H] was fixed to a typical M-dwarf metallicity of -0.5. We fixed the extinction $(A_{\rm V})$ to zero, considering the proximity of the star and that the degrees-of-freedom of the fit is 10. The resulting fit (Fig. 1) has a χ^2 of 42.3 ($\chi^2_{\rm red}$ = 4.2), with $T_{\rm eff}$ = 3800 ± 70 K. The relatively high χ^2 is likely due to systematics since the stellar atmosphere model is not perfect. We artificially increased the observational uncertainty estimates until $\chi^2_{\text{red}} = 1$ was achieved. Integrating the (unreddened) model SED gives the bolometric flux at Earth of $F_{\rm bol} = 3.41 \pm 0.12 \times 10^{-9}$ erg s⁻¹ cm⁻². By taking the $F_{\rm bol}$ and $T_{\rm eff}$ together with the *Gaia* DR2 parallax, which was adjusted by +0.08 mas to account for the systematic offset reported by Stassun & Torres (2018), this gives the stellar radius of $R = 0.600 \pm 0.022 R_{\odot}$. Finally, estimating the stellar mass from the empirical relations of Mann et al. (2019) gives $M = 0.62 \pm 0.03 M_{\odot}$. With these values for the mass and radius, the stellar mean density is $\rho = 4.04 \pm 0.49 \text{ g cm}^{-3}$. We also tested to fit the SED by using a BT-Settl theoretical grid of stellar model (Allard 2014), where we obtained a consistent

We searched for infrared (IR) excess in WISE data using the Virtual Observatory SED Analyser (VOSA, Bayo et al. 2008), which could indicate the presence of debris disks. We computed the excess significance parameter (χ_{λ} , Beichman et al. 2006;

Table 1. L 168-9 (TIC 234994474) properties.

| Parameter | Units | Value | Reference |
|-----------------------------|----------------------|-------------------------|-----------|
| RA | [J2000] | $23^{h}20^{m}07.52^{s}$ | Gaia2018 |
| Dec | [J2000] | -60°03′54.64″ | Gaia2018 |
| Spectral type | | M1V | Ga2014 |
| B | [mag] | 12.45 ± 0.19 | Ho2000 |
| V | [mag] | 11.02 ± 0.06 | Ho2000 |
| $B_{ m A}$ | [mag] | 12.460 ± 0.025 | He2016 |
| $V_{ m A}$ | [mag] | 11.005 ± 0.018 | He2016 |
| $g_{ m A}$ | [mag] | 11.752 ± 0.032 | He2016 |
| $R_{\rm A}$ | [mag] | 10.416 ± 0.028 | He2016 |
| $i_{ m A}$ | [mag] | 9.675 | He2016 |
| W_1 | [mag] | 6.928 ± 0.060 | Cu2013 |
| W_2 | [mag] | 6.984 ± 0.020 | Cu2013 |
| W_3 | [mag] | 6.906 ± 0.016 | Cu2013 |
| W_4 | [mag] | 6.897 ± 0.074 | Cu2013 |
| T | | 9.2298 ± 0.0073 | St2018 |
| J | | 7.941 ± 0.019 | Cu2003 |
| H | | 7.320 ± 0.053 | Cu2003 |
| K_{s} | | 7.082 ± 0.031 | Cu2003 |
| B_{p} | | 11.2811 ± 0.0016 | Gaia2018 |
| \vec{G} | | 10.2316 ± 0.0008 | Gaia2018 |
| R_{p} | | 9.2523 ± 0.0011 | Gaia2018 |
| π | [mas] | 39.762 ± 0.038 | Gaia2018 |
| Distance | [pc] | 25.150 ± 0.024 | Gaia2018 |
| μ_{lpha} | $[mas yr^{-1}]$ | -319.96 ± 0.10 | Gaia2018 |
| μ_δ | $[mas yr^{-1}]$ | -127.78 ± 0.12 | Gaia2018 |
| $\mathrm{d}v_r/\mathrm{d}t$ | $[m s^{-1} yr^{-1}]$ | 0.06865 ± 0.00011 | this work |
| M_{s} | $[M_{\odot}]$ | 0.62 ± 0.03 | Ma2019 |
| $R_{\rm s}$ | $[R_{\odot}]$ | 0.600 ± 0.022 | Sect. 2 |
| $T_{ m eff}$ | [K] | 3800 ± 70 | Sect. 2 |
| $L_{\rm s}$ | $[L_{\odot}]$ | 0.0673 ± 0.0024 | Sect. 2 |
| $\log(g)$ | $[g cm^{-3}]$ | 4.04 ± 0.49 | Sect. 2 |
| [Fe/H] | | 0.04 ± 0.17 | Ne2014 |
| $\log(R'_{\rm HK})$ | | -4.562 ± 0.043 | As2017A |
| $P_{\rm rot}$ | [days] | 29.8 ± 1.3 | Sect. 4.1 |

References. Gaia2018 – Gaia Collaboration (2018); Ga2014 – Gaidos et al. (2014); Ho2000 – Høg et al. (2000); H22016 – Henden et al. (2016); Cu2013 – Cutri et al. (2013); St2018 – Stassun et al. (2018b); Cu2003 – Cutri et al. (2003); Ma2019 – Mann et al. (2019); Ne2014 – Neves et al. (2014); As2017a – Astudillo-Defru et al. (2017a).

Moór et al. 2006) in which $\chi_{\lambda} \ge 3$ represents a robust detection of IR excess. We obtained $\chi_{\lambda} = 0.70$ in the W_3 band, ruling out the presence of a debris disk around L 168-9.

3. Observations

The first hint of a planetary companion orbiting L 168-9 came about following the analysis of TESS data. After the data validation report was released to the community, a follow-up campaign started with several instruments and was performed by different teams to check on whether the transit-like signal seen by TESS originated from a planet, as opposed to a stellar binary or other source. The follow-up observations included supplementary time series photometry aiming to detect additional transits, seeing-limited and high-resolution imaging to analyze the possibility that the signal comes from a star on a nearby sightline, and precise radial-velocity monitoring to measure the companion's mass.

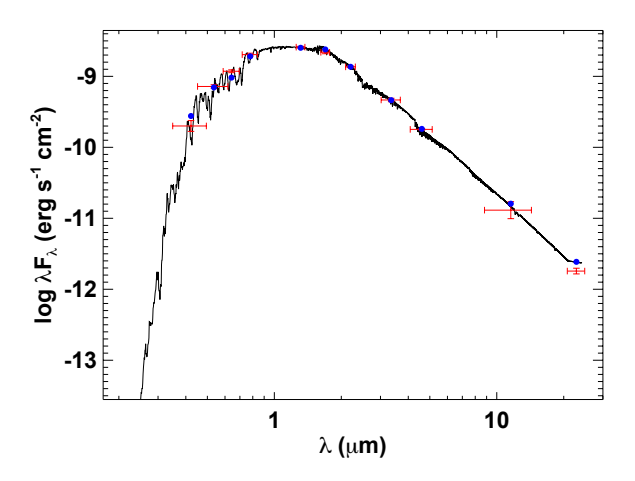


Fig. 1. Spectral energy distribution (SED) of L 168-9. Red error bars represent the observed photometric measurements, where the horizontal bars represent the effective width of the passband. Blue circles are the model fluxes from the best-fit NextGen atmosphere model (black).

3.1. Photometry

3.1.1. TESS

TESS observed Sector 1 from 25 July to 22 August 2018^1 , a 27.4-day interval that is typical of each sector. L 168-9 is listed in the cool dwarf catalog, for which the known properties of as many dwarf stars as possible with V-J>2.7 and effective temperatures lower than 4000 K were gathered (Muirhead et al. 2018). The predicted TESS-band apparent magnitudes are also given in this catalog. L 168-9 was chosen for 2-min time sampling as part of the TESS candidate target list (CTL, Stassun et al. 2018b), consisting of a subset of the TIC identified as high-priority stars in the search for small transiting planets. Time series observations of L 168-9 were made with CCD 2 of Camera 2.

The basic calibration, reduction, and detrending of the time series as well as the search for transit-like signals were performed in the TESS Science Processing Operations Center (SPOC) at the NASA Ames Research Center (Jenkins et al. 2016). The light curves were derived by the SPOC pipeline, and they consist of a time series based on simple aperture photometry (SAP) as well as a corrected time series based on presearch data conditioning (PDC, Smith et al. 2012; Stumpe et al. 2014) referred to as PDCSAP (as detailed in the TESS Science Data Products Description Document²). This work made use of the PDC-SAP time series available on the Mikulski Archive for Space Telescopes (MAST³).

A data validation report for L 168-9 was released to the community as part of the MIT TESS alerts⁴. The report includes several of the following validation tests to assess the probability that the signal is a false positive: eclipsing-binary discrimination tests, a statistical bootstrap test, a ghost diagnostic test, and difference-image centroid offset tests. These are described by Twicken et al. (2018). All of the tests were performed successfully. The formal false-alarm probability of the planet candidate was reported to be 5.85×10^{-37} .

The TESS time series covers 19 transits for what was originally deemed a planet candidate (L 168-9 b or TOI-134.01), and it was reported on the TESS exoplanet follow-up observing program (TFOP) website⁵. According to the data validation report, the orbital period is $P=1.401461\pm0.000137$ days and the transit depth is $\Delta F/F_0=566\pm38$ ppm, which translates into a planetary radius of $R_p=1.58\pm0.36$ R_\oplus (Sect. 2 describes how we determined the stellar radius, which is the same value as the one used in the validation report). The time of midtransit at an arbitrarily chosen reference epoch is (BJD) $T_c=2458326.0332\pm0.0015$.

3.1.2. LCOGT, MKO, and SSO T17

We acquired ground-based time series photometric follow-up of L 168-9 and the nearby field stars as part of the TESS follow-up observing program (TFOP) to attempt to rule out nearby eclipsing binaries (NEBs) in all stars that are bright enough to cause the TESS detection and that could be blended in the TESS aperture. We used the TESS Transit Finder⁶, which is a customized version of the Tapir software package (Jensen 2013), to schedule our transit observations.

We observed one full transit simultaneously by using three 1-m telescopes at the Las Cumbres Observatory Global Telescope (LCOGT; Brown et al. 2013) South Africa Astronomical Observatory node on 21 September 2018 in the i'-band. The Sinistro detectors consist of 4K×4K 15- μ m pixels with an image scale of 0. 389 pixel⁻¹, resulting in a field-of-view of 26.5 × 26.5. The images were calibrated by the standard LCOGT BANZAI pipeline.

We observed a full transit from the Mount Kent Observatory (MKO) 0.7-m telescope near Toowoomba, Australia on 23 September 2018 in the r'-band. The Apogee U16 detector consists of $4K \times 4K$ 9- μ m pixels with an image scale of 0'.41 pixel⁻¹, resulting in a field-of-view of $27' \times 27'$. The images were calibrated using the AstroImageJ (AIJ) software package (Collins et al. 2017).

We observed a full transit from the Siding Spring Observatory, Australia, iTelescope T17 0.43-m telescope on 27 September 2018 with no filter. The FLI ProLine PL4710 detector consists of $1K\times1K$ pixels with an image scale of 0.92 pixel-1, resulting in a field-of-view of 15.5×15.5 . The images were calibrated using AstroImageJ.

We used the AstroImageJ to extract differential light curves of L 168-9 and all known stars within 2.5 of the target star that are bright enough to have possibly produced the shallow TESS detection, which includes 11 neighbors brighter than TESS-band = 17.9 mag. This allows an extra 0.5 in delta magnitude relative to L 168-9 to account for any inaccuracies in the TESS band reported magnitudes in the TICv8. The L 168-9 light curves in all five photometric data sets show no significant detection of the shallow TESS detected event, which is as expected from our lower precision ground-based photometry. Considering a combination of all five photometric data sets, we excluded all 11 known neighbors that are close enough and bright enough to L 168-9 to have possibly caused the TESS detection as potential sources of the TESS detection.

3.1.3. WASP

WASP-South, located in Sutherland, South Africa, is the southern station of the Wide Angle Search for Planets (WASP,

 $^{^1}$ The Sector 1 pointing direction was RA(J2000):+352.68°, Dec(J2000):-64.85°, Roll:-137.85°.

https://archive.stsci.edu/missions/tess/doc/ EXP-TESS-ARC-ICD-TM-0014.pdf

³ https://mast.stsci.edu/portal/Mashup/Clients/Mast/ Portal.html

⁴ https://tev.mit.edu

⁵ https://exofop.ipac.caltech.edu/tess/

⁶ https://astro.swarthmore.edu/telescope/tess-secure/ find_tess_transits.cgi

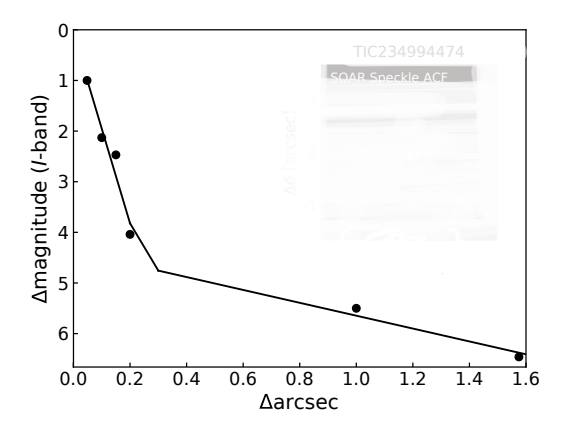


Fig. 2. SOAR speckle results of L 168-9. Black points represent the I-band contrast obtained at a given separation of the star. The solid black line shows the 5σ detection limit curve.

Pollacco et al. 2006). It consists of an array of eight cameras, each of which is backed by a 2048 × 2048 CCD. Observations in 2010 and 2011 (season A) used 200 mm, f/1.8 lenses with a broadband filter spanning 400–700 nm and a plate scale of 13.7" pixel⁻¹. Then, from 2012 to 2014 (season B), WASP-South used 85 mm, f/1.2 lenses with a Sloan r' filter and a plate scale of 32" pixel⁻¹. The array rastered a number of fields during a clear night at typically 10-min cadence.

L 168-9 was monitored for four consecutive years, from 20 May 2010 to 12 December 2014; typically covering 150 days in each year. In one campaign, two cameras with overlapping fields observed the star, giving a total of 27 300 data points; in another campaign, L 168-9 was observed by three cameras with overlapping fields, totaling 170 000 data points. The photometry has a dispersion of 0.027 δ mag and an average uncertainty of 0.024 δ mag, presenting clear signs of variability, as shown below in Sect. 4.1.

3.2. High-resolution imaging

The relatively large 21" pixels of TESS can lead to photometric contamination from nearby sources. These must be accounted for to rule out astrophysical false positives, such as background eclipsing binaries, and to correct the estimated planetary radius, which was initially derived from the diluted transit in a blended light curve (Ziegler et al. 2018). Without this correction, the interpreted planet radius can be underestimated (e.g., Ciardi et al. 2015; Teske et al. 2018).

3.2.1. SOAR

We searched for close companions to L 168-9 with speckle imaging on the 4.1-m Southern Astrophysical Research telescope (SOAR, Tokovinin 2018) installed in Cerro Pachón, Chile, on 2018 September 25 UT using the *I*-band ($\lambda_{\rm cen}=824\,$ nm, full width at half maximum = 170 nm) centered approximately on the TESS passband. Further details of the TESS SOAR survey are published in Ziegler et al. (2020).

Figure 2 shows the 5σ detection sensitivity. No nearby stars (ρ < 1".6) to L 168-9 were detected within the sensitivity limits of SOAR.

3.2.2. Gemini-South

Observations of L 168-9 were conducted with the Differential Speckle Survey Instrument (DSSI; Horch et al. 2009) on Gemini

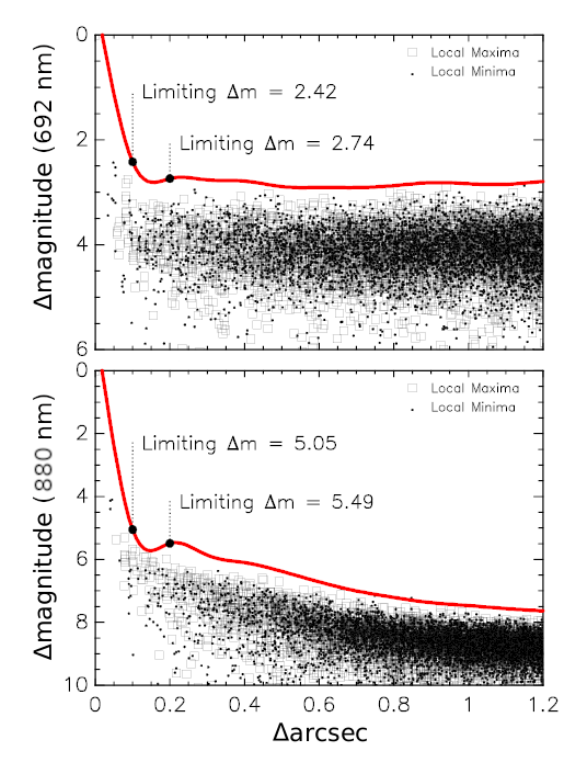


Fig. 3. DSSI/Gemini-S detection limit curves of L 168-9 in the 692 nm (*top*) and 880 nm (*bottom*) filters. Squares and points on the left represent local maxima and local minima, respectively.

South, Chile, on UT 28 October 2018 under program GS-2018B-LP-101 (PI: I. Crossfield). The usual 692 nm and 880 nm filters on DSSI were used, and three sequences of 60 ms/frame×1000 frames were taken. The total time on target, including readout overhead, was six minutes. Howell et al. (2011) and Horch et al. (2011, 2012) detail the speckle observing and data reduction procedures. The detection limit curves are shown in Fig. 3. While the 692 nm image was taken at too low of a gain, leading to a shallow detection limit, the 880 nm detection limit curve (b) in Fig. 3 indicates that L 168-9 lacks any companions of $\Delta m \sim 5.0$ mag beyond 0.1" and any companions of $\Delta m \sim 5.5$ mag beyond 0.2". Gemini-South and the SOAR result (Sect. 3.2.1) means that the transit signal is likely to be associated with L 168-9.

Thus, we conclude that there is no significant contamination of the TESS photometric aperture that would bias the determination of the planet radius. The Sinistro data (Sect. 3.1.2) rule out surrounding stars as potential sources of the TESS detection, so we can assume the planet orbits L 168-9. Given the limits placed on nearby companions by the Gemini-South data, if there were a close companion, it would have to be fainter by ~5 magnitudes than the primary star, meaning the planet radius correction factor would be at most

$$R_{\rm p,corr} = R_{\rm p} \times \sqrt{1 + 10^{-0.4\Delta m}} = R_{\rm p} \times 1.005.$$
 (1)

This is smaller than the derived planet radius uncertainty (Table 2).

3.3. Radial velocity

3.3.1. HARPS

The High Accuracy Radial velocity Planet Searcher (HARPS Mayor et al. 2003) is an echelle spectrograph that is mounted

Table 2. Measured transit and RV model parameters of the L 168-9 planetary system.

| Measured transit model parameters | TESS | | | | | | |
|---|-------------------------|------------------------------------|-------------------------|--|--|--|--|
| Baseline flux, γ_{TESS} | 0.00001 ± 0.00029 | | | | | | |
| Orbital period, P_b [days] | 1.40150 ± 0.00018 | | | | | | |
| Time of midtransit, T_0 [BJD-2,457,000] | | $1340.04781^{+0.00088}_{-0.00122}$ | | | | | |
| Scaled semimajor axis, a/R_s | | 7.61 ± 0.31 | | | | | |
| Planet-star radius ratio, r_p/R_s | | 0.0212 ± 0.001 | | | | | |
| Orbital inclination, i [deg] | | $85.5^{+0.8}_{-0.7}$ | | | | | |
| Linear limb darkening coefficient, q_1 | | $0.397^{+0.125}_{-0.111}$ | | | | | |
| Quadratic limb darkening coefficient, q_2 | | $0.189^{+0.058}_{-0.056}$ | | | | | |
| TESS additive jitter, s_{TESS} | | $0.00003^{+0.00011}_{-0.00003}$ | | | | | |
| Radial velocity GP hyperparameters | HARPS+PFS | HARPS | PFS | | | | |
| $\overline{\ln \text{HARPS covariance amplitude, } \ln (a_{\text{HARPS}}/\text{m s}^{-1})}$ | $3.27^{+1.38}_{-1.03}$ | $3.24_{-1.19}^{+1.24}$ | - | | | | |
| ln PFS covariance amplitude, $\ln (a_{PFS}/\text{m s}^{-1})$ | $3.63^{+1.24}_{-1.08}$ | - | $4.01^{+1.23}_{-0.97}$ | | | | |
| ln RV exponential timescale, $\ln (\lambda_{RV}/\text{day})$ | $11.90^{+2.81}_{-1.99}$ | $12.25^{+3.16}_{-2.18}$ | $13.3^{+2.02}_{-1.44}$ | | | | |
| $\ln RV$ coherence, $\ln (\Gamma_{RV})$ | $-0.09^{+0.20}_{-0.24}$ | $-0.42^{+0.41}_{-0.55}$ | $-0.22^{+0.39}_{-0.44}$ | | | | |
| $\ln RV$ periodic timescale, $\ln (P_{RV}/\text{day})$ | $3.47^{+0.02}_{-0.03}$ | $3.47^{+0.03}_{-0.03}$ | $3.48^{+0.04}_{-0.03}$ | | | | |
| HARPS additive jitter, s_{HARPS} [m s ⁻¹] | $0.10^{+0.20}_{-0.09}$ | $0.86^{+0.98}_{-0.86}$ | - | | | | |
| PFS additive jitter, s_{PFS} [m s ⁻¹] | 2.82 ± 0.42 | - | 2.78 ± 0.30 | | | | |
| Measured RV model parameters | HARPS+PFS | HARPS | PFS | | | | |
| HARPS zero point velocity, γ_{HARPS} [km s ⁻¹] | 29.7687 ± 0.0013 | 29.7692 ± 0.0013 | - | | | | |
| PFS zero point velocity, γ_{PFS} [km s ⁻¹] | 0.00077 ± 0.00186 | - | 0.00063 ± 0.00142 | | | | |
| Semiamplitude, K [m s ⁻¹] | $3.66^{+0.47}_{-0.46}$ | $3.74^{+0.54}_{-0.59}$ | $3.26^{+0.52}_{-0.70}$ | | | | |
| $h = \sqrt{e}\cos\omega$ | $-0.10^{+0.17}_{-0.12}$ | $0.04^{+0.15}_{-0.18}$ | $-0.01^{+0.18}_{-0.21}$ | | | | |
| $k = \sqrt{e} \sin \omega$ | $0.00^{+0.17}_{-0.16}$ | $-0.09^{+0.22}_{-0.23}$ | $0.01^{+0.23}_{-0.30}$ | | | | |
| Derived L 168-9 b parameters | HARPS+PFS+TESS | HARPS+TESS | PFS+TESS | | | | |
| Semimajor axis, a [AU] | 0.02091 ± 0.00024 | | | | | | |
| Equilibrium temperature, $T_{\rm eq}$ [K] | | | | | | | |
| Zero bond albedo | 965 ± 20 | | | | | | |
| Venus-like bond albedo = 0.77 | 668 ± 14 | | | | | | |
| Planetary radius, R_p [R_{\oplus}] | 1.39 ± 0.09 | | | | | | |
| Planetary mass, M_p [M_{\oplus}] | 4.60 ± 0.56 | $4.74^{+0.71}_{-0.75}$ | $4.08^{+0.70}_{-0.90}$ | | | | |
| Planetary bulk density, $ ho_{ m p}$ [g cm $^{-3}$] | $9.6^{+2.4}_{-1.8}$ | $10.0^{+2.5}_{-1.9}$ | $8.7^{+2.3}_{-2.1}$ | | | | |
| Planetary surface gravity, $g_{\rm p}~{\rm [m~s^{-2}]}$ | $23.9^{+4.5}_{-3.9}$ | $24.4^{+4.8}_{-4.2}$ | $21.4^{+4.4}_{-4.8}$ | | | | |
| Planetary escape velocity, $v_{\rm esc}$ [km s ⁻¹] | $20.5^{+1.4}_{-1.4}$ | $20.8^{+1.6}_{-1.7}$ | $19.4^{+1.6}_{-2.2}$ | | | | |
| Orbital eccentricity, $e^{(\dagger)}$ | < 0.21 | < 0.25 | < 0.26 | | | | |

Notes. (†)95% confidence interval.

on the 3.6 m telescope at La Silla Observatory, Chile. The light is spread over two CCDs (pixel size 15 μ m) by a science fiber and a calibration fiber. The calibration fiber can be illuminated with the calibration lamp for the best radial velocity precision,

or it can be placed on sky for moderate precision. HARPS is stabilized in pressure and temperature, and it has a resolving power of 115 000. The achievable precision in radial velocity is better than $1~{\rm m\,s^{-1}}$.

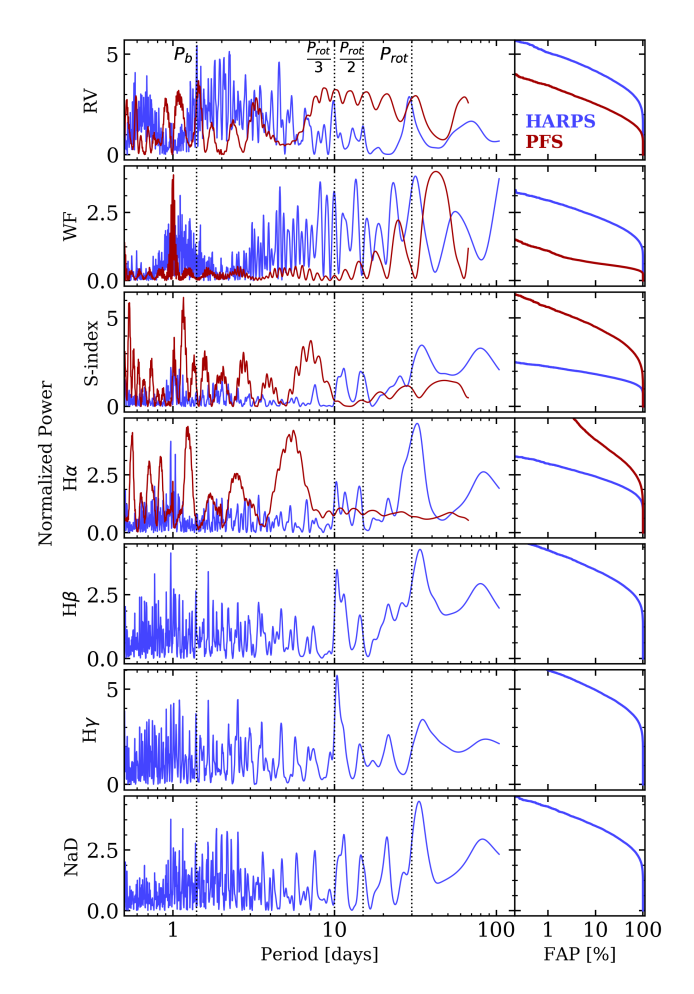


Fig. 4. Left column: generalized Lomb-Scargle periodograms of the HARPS and PFS RV time series, window functions, and the S-index, $H\alpha$, $H\beta$, $H\gamma$, and sodium doublet activity indicators. The vertical dotted lines highlight the locations of the L 168-9 b orbital period, the stellar rotation period, and its first two harmonics. Right column: false alarm probabilities were computed from bootstrapping with replacement.

We began monitoring L 168-9 with HARPS on 29 September 2018, which was soon after the TESS alert. We elected not to use the simultaneous wavelength calibration (i.e., the on-sky calibration fiber) to ensure that the bluer spectral regions would not be contaminated by the calibration lamp that provides a much stronger flux for any instrumental setup. The exposure time was set to 900 s for ESO programs 198.C-0838 and 1102.C-0339, and to 1200 s for ESO program 0101.C-0510, translating in a median signal-to-noise ratio (S/N) per spectral pixel of 51 and 70 at 650 nm, respectively. A single spectrum on 1 October 2018 had an exposure time of 609 s for an unknown reason. A total of 47 HARPS spectra were collected, ending with observations on 19 December 2018.

HARPS spectra were acquired in roughly three packs of data separated in time by about 40 days. This sampling is reflected in the window function presented in Fig. 4. Two archival spectra of L 168-9 are available at the ESO database. However, a radial velocity offset was introduced in May 2015 because the vacuum vessel was opened during a fiber upgrade (Lo Curto et al. 2015). As this offset is not yet well characterized for M dwarfs, we decided to disregard those two points (from July 2008 and June 2009) in our subsequent analysis.

The HARPS Data Reduction Software (Lovis & Pepe 2007) computes radial velocities by a cross-correlation function

technique (e.g., Baranne et al. 1996). Nevertheless, we derived radial velocities with a different approach to exploit the Doppler information of spectra as much as possible (e.g., Anglada-Escudé & Butler 2012). We performed a maximum likelihood analysis between a stellar template and each individual spectrum following the procedure presented in Astudillo-Defru et al. (2017b). The stellar template corresponds to a true stellar spectrum of the star in which the signal-to-noise ratio is enhanced. It was made from the median of all the spectra after shifting them into a common barycentric frame. The resulting template is Doppler shifted by a range of trial radial velocities to construct the maximum likelihood function from which we derived the HARPS radial velocity used in the subsequent analysis. The obtained radial velocities, which are listed in Table B.1, present a dispersion of 4.01 m s⁻¹ and a median photon uncertainty of 1.71 m s^{-1} .

3.3.2. PFS

The Planet Finder Spectrograph is an iodine-calibrated, environmentally controlled high resolution PRV spectrograph (Crane et al. 2006, 2008, 2010). Since first light in October 2009, PFS has been running a long-term survey program to search for planets around nearby stars (e.g., Teske et al. 2016). In January 2018, PFS was upgraded with a new large format CCD with 9μ m pixels and switched to a narrower slit for its regular operation mode to boost the resolution from 80 000 to 130 000. The PFS spectra were reduced and analyzed with a custom IDL pipeline that is capable of delivering RVs with <1 m s⁻¹ precision (Butler et al. 1996).

We followed up L 168-9 with PFS on the 6.5 m Magellan II Clay telescope at Las Campanas Observatory in Chile from 13-26 October 2018 and then on 16 and 21 December 2018. Observations were conducted on 15 nights, with multiple exposures per night. There were a total of 76 exposures of 20 min each. We typically took 2-6 exposures per night over a range of timescales to increase the total S/N per epoch and also to average out the stellar and instrumental jitter. Each exposure had a typical S/N of 28 per pixel near the peak of the blaze function, or 56 per resolution element. The radial velocity dispersion is 4.61 m s⁻¹ and the median RV uncertainty per exposure is about 1.8 m s⁻¹. Five consecutive 20-min iodine-free exposures were obtained to allow for the construction of a stellar spectral template in order to extract the RVs. These were bracketed with spectra of rapidly rotating B stars taken through the iodine cell for reconstruction of the spectral line spread function and wavelength calibration for the template observations.

The PFS observations of L 168-9 that are presented here are part of the *Magellan* TESS survey (MTS) that will follow up on ~30 super-Earths and sub-Neptunes discovered by TESS in the next three years using PFS (Teske et al., in prep.). The goal of MTS is to conduct a statistically robust survey to understand the formation and evolution of super-Earths and sub-Neptunes. The observation schedules of all MTS targets, including L 168-9, can be found on the ExoFOP-TESS website⁷.

4. Analysis

4.1. Photometric rotation period

Knowledge of the stellar rotation period helps to disentangle spurious RV signals arising from rotation and true RV signals due

⁷ https://exofop.ipac.caltech.edu/tess/

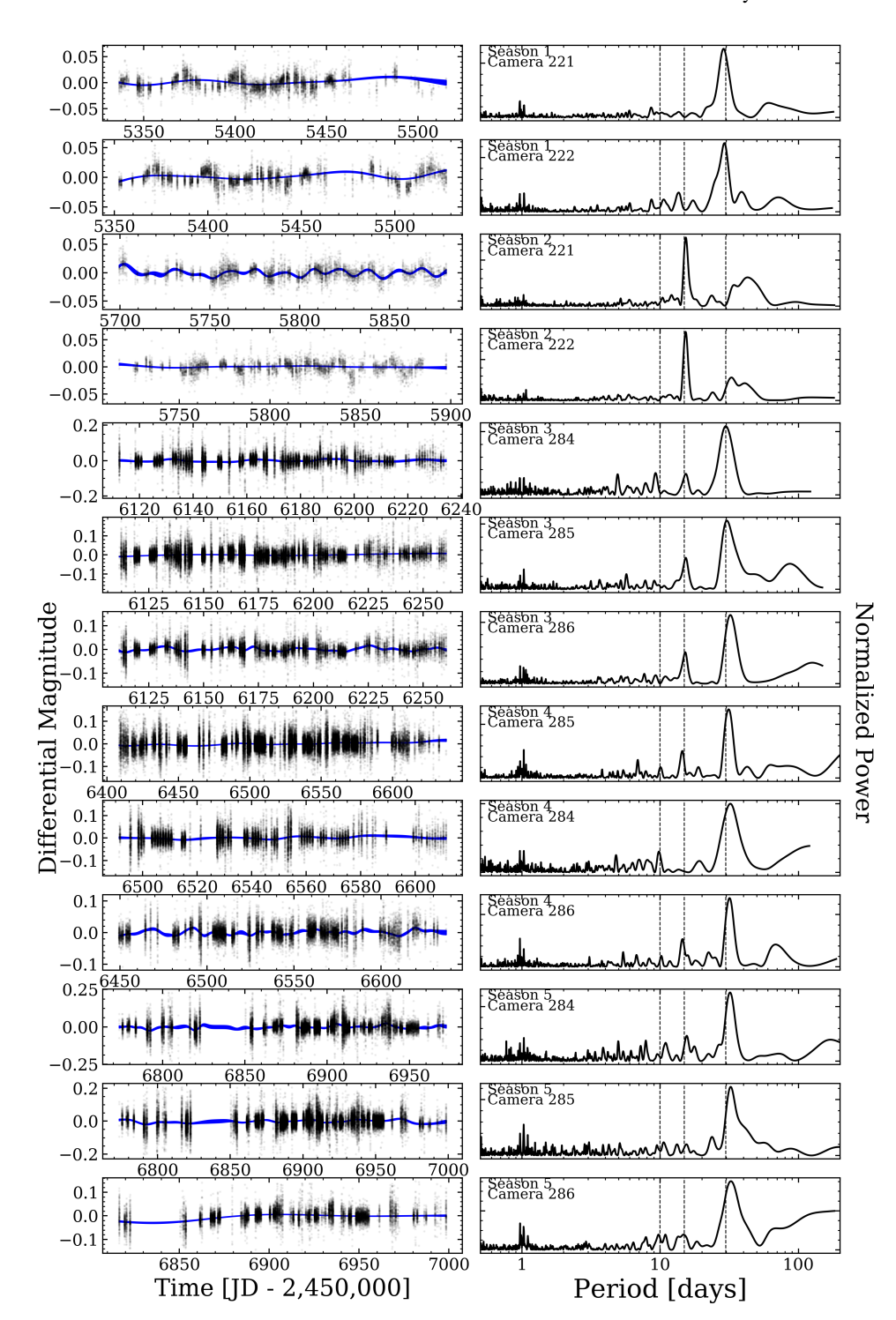


Fig. 5. WASP photometry. Left column: photometry time series; the blue shaded regions depict $\pm 1\sigma$ about the mean GP regression model of the binned photometry. Right column: generalized Lomb-Scargle periodogram of each season highlights the prevalence of photometric variations close to the measured rotation period and/or its first and second harmonics (vertical dashed lines).

to orbital motion (e.g., Queloz et al. 2001; Cloutier et al. 2017). L 168-9 was photometrically monitored by WASP between May 2010 and December 2014 within five observing seasons, each lasting approximately 200 days in duration. The photometric precision, observing cadence, and baselines within the WASP fields are sufficient to detect quasi-periodic (QP) photometric variations of L 168-9 due to active regions on the stellar surface rotating in and out of view at the stellar rotation period $P_{\rm rot}$. The WASP photometry of L 168-9 is shown in Fig. 5 along with the generalized Lomb-Scargle periodogram (GLSP; Zechmeister & Kürster 2009) of the photometry in each of the five WASP observing seasons. It is clear from the GLSPs that a strong periodicity exists within the data whose timescale is often ~30 days,

except for within the second WASP season wherein the dominant periodicity appears at the first harmonic of $P_{\text{rot}} \sim 15$ days.

Given periodicities that are significantly detected in the WASP photometry, we proceeded to measure the photometric rotation period of L 168-9 P_{rot} with each WASP camera and in each WASP field⁸ in which L 168-9 was observed. As the photometric variations appear to vary nearly periodically, we modeled the photometry with a Gaussian process (GP) regression model and adopted a QP covariance kernel (see Eq. (A.1)) (Angus et al. 2018). The covariance function's periodic timescale was a free

 $^{^{8}}$ At times, L 168-9 appeared within the fields-of-view of multiple WASP cameras.

parameter $P_{\rm rot}$ for which the posterior probability density function (PDF) was sampled using a Markov chain Monte Carlo (MCMC) method (see Appendix A). We modeled each binned WASP light curve with a GP. We adopted a bin size of 1 day to reduce the computation time. In preliminary analyses, we also tested bin sizes of 0.25, 0.5, and 2 days and found that the recovered values of $P_{\rm rot}$ were not very sensitive to this choice, which is probably due to the very large number of points.

After sampling the posterior PDFs of the GP hyperparameters, we obtained point estimates for each parameter value based on the maximum a-posteriori values and 68 percent confidence intervals. The resulting mean GP model of the data from each WASP observing season is depicted in Fig. 5 along with the corresponding 1σ confidence interval. Over the five observing seasons, the measured (median) rotation period of L 168-9 was $P_{\rm rot} = 29.8 \pm 1.3$ days.

In principle, the WASP signal could have arisen from any star within the 48" extraction aperture. However, L 168-9 is the brightest star in the aperture by far. Another concern with any photometric signal with a period near 30 days is whether it was affected by moonlight. To check on this possibility, we searched for modulations in the WASP data of several stars with a similar brightness within the surrounding 10 arcmin field, but we did not find any 30-d signals similar to the one that was seen for L 168-9. In any case, the star location is far from the ecliptic, and moonlight contamination is not expected. Furthermore, the modulation was sometimes seen at the 15-d first harmonic, which would not be expected for moonlight. We can therefore be confident that the 30-d periodicity in the WASP data arises from L 168-9. The $R'_{\rm HK}$ from HARPS spectra supports the obtained photometric rotation period, as $log(R'_{HK}) =$ -4.562 ± 0.043 (active star) translates into $P_{\text{rot}} = 22 \pm 2$ days using the R'_{HK} versus P_{rot} relationship from Astudillo-Defru et al. (2017a).

4.2. Radial velocity periodogram analysis

A first identification of significant periodicities in the HARPS and PFS RV time series is required in order to develop an accurate model of the observed RV variations. In a manner similar to our analysis of the WASP photometry, we computed the GLSP of the following HARPS and PFS spectroscopic time series: the RVs, the window functions (WF), and the S-index, $H\alpha$, $H\beta$, $H\gamma$, and the sodium doublet NaD activity indicators. Astudillo-Defru et al. (2017b) detail how these spectroscopic activity indicators were derived. Each GLSP is shown in Fig. 4 along with a false alarm probability (FAP) that was computed via bootstrapping with replacement using 10^4 iterations and normalizing each periodogram by its standard deviation.

Each of the GLSPs of the HARPS and PFS RV time series is dominated by noise and aliases arising from the respective WF. For example, the HARPS WF contains a forest of peaks with comparable FAP from ~ 8 days and extending out toward long periodicities. Similarly the GLSP of the PFS WF reveals a series of broad peaks for periodicities $\gtrsim 1$ day. These features, particularly those from the PFS WF, have clear manifestations in the GLSPs of their respective RV and activity indicator time series, thereby complicating the robust identification of periodocities in the data. However, strong peaks at the orbital period of L 168-9 b (~ 1.4 days) are discernible in both RV time series at FAP $\sim 0.4\%$ and $\sim 0.3\%$ with HARPS and PFS, respectively. This periodicity is not apparent in any of the ancillary activity indicator time series, which is expected for a signal originating from an orbiting planet.

In addition to the signal from L 168-9 b, the HARPS RVs exhibit some power close to $P_{\rm rot}$ and its second harmonic $P_{\rm rot}/3$. Although the FAPs of these periodicities over the full frequency domain are large, they each appear locally as strong periodicities since most of the power in the HARPS RVs exists at $\lesssim 5$ days. The GLSP of the PFS RVs is much more difficult to interpret at periodicities in the vicinity of $P_{\rm rot}$ and its first and second harmonics due to strong aliases from the PFS WF. Due to these effects, it is difficult to discern from the available PFS activity indices (i.e., S-index and $H\alpha$) whether or not a coherent activity signal is seen with PFS. Although each of the HARPS and PFS RV time series are significantly affected by sampling aliases, we do see evidence for L 168-9 b and rotationally modulated stellar activity in the RVs we endeavor to mitigate with our adopted model discussed in Sect. 4.3.

4.3. Radial velocity and transit model

Guided by the periodicities in the HARPS and PFS RV time series, we proceeded to fit a model to the RVs including the effects of both stellar activity and the planet. Following numerous successful applications on both Sun-like (e.g., Haywood et al. 2014; Grunblatt et al. 2015; Faria et al. 2016; López-Morales et al. 2016; Mortier et al. 2016) and M dwarf stars (e.g., Astudillo-Defru et al. 2017c; Bonfils et al. 2018; Cloutier et al. 2019a; Ment et al. 2019), we adopted a QP kernel for the GP as a nonparametric model of the physical processes resulting in stellar activity. When used to model RV stellar activity, the QP covariance kernel is often interpreted to model the rotational component of stellar activity from active regions on the rotating stellar surface whose lifetimes typically exceed many rotation cycles on M dwarfs (Giles et al. 2017) plus the evolutionary time scale of the active regions. The corresponding GP hyperparameters are described in detail in Appendix A and include each spectrograph's covariance amplitudes a_{HARPS} , a_{PFS} , the common exponential timescale λ_{RV} , the common coherence parameter Γ_{RV} , and the common periodic timescale P_{RV} equal to the stellar rotation period P_{rot} .

The planetary component that is attributed to the transiting planet L 168-9 b was fit to the detrended light curve with a Mandel & Agol (2002) planetary transit model. The detrended TESS light curve was produced by adjusting a QP GP systematic model to the photometry alone and with all the transits previously removed. The best OP GP model was subtracted to the entire TESS data set. The planetary component is modeled by a Keplerian solution that is parameterized by the planet's orbital period P_b , time of midtransit T_0 , RV semiamplitude K, and the orbital parameters $h = \sqrt{e} \cos \omega$ and $k = \sqrt{e} \sin \omega$ where e and ω are the planet's orbital eccentricity and argument of periastron, respectively. In addition, our RV model contains each spectrograph's zero point velocity γ_{HARPS} , γ_{PFS} and an additive scalar jitter s_{HARPS} , s_{PFS} that accounts for any residual jitter that, unlike the stellar activity signal, is not temporally correlated. The complete RV model therefore contains fourteen model parameters.

To ensure self-consistent planet solutions between the available TESS transit data and the RV observations, we simultaneously fit the detrended light curve and the RVs. The common planetary parameters between these two data sets are P_b , T_0 , h, and k. The additional model parameters that are required to model the TESS transit light curve included an additive scalar jitter $s_{\rm TESS}$, the baseline flux $\gamma_{\rm TESS}$, the scaled semimajor axis a/R_s , the planet-star radius ratio r_p/R_s , the orbital inclination i, and the nearly-uncorrelated parameters q_1 and q_2 , which are

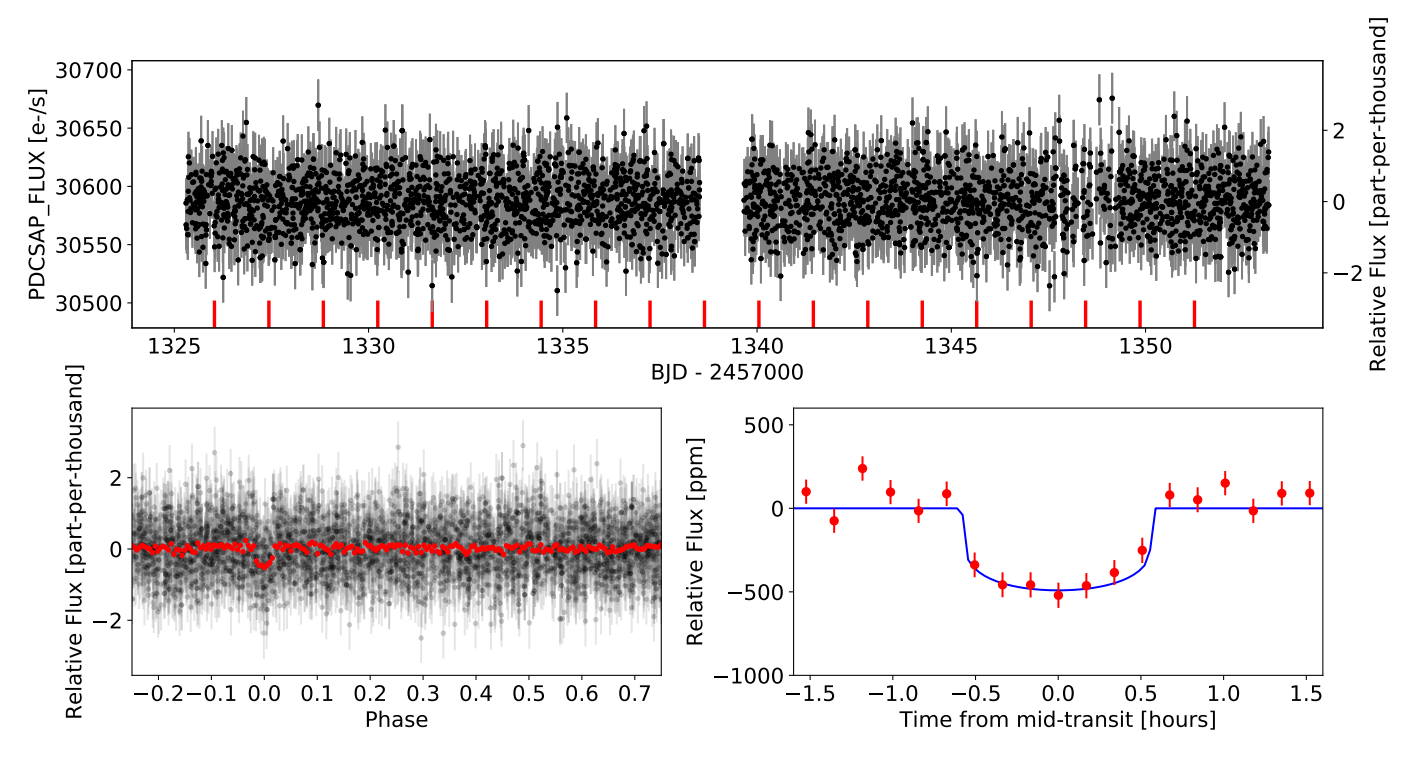


Fig. 6. Time series of TESS data for L 168-9. One fifth of original data are plotted for visualization purposes. *Upper panel*: detrended TESS light curve. Red vertical bars represent the transits of the planet candidate. *Bottom panel*: phase folded normalized photometry. Red points correspond to binned data for illustrative purposes. The entire orbital phase is shown to the left, while the right presents the transit phase as well as the best transit model whose parameters come from the Table 2.

related to the quadratic limb darkening coefficients u_1 and u_2 via

$$q_1 = (u_1 + u_2)^2 (2)$$

$$q_2 = \frac{u_1}{2(u_1 + u_2)} \tag{3}$$

(Kipping 2013). Thus we required eleven model parameters to describe the TESS transit light curve and a total of twenty-one model parameters of the joint RV and light curve data set: $\Theta = \{a_{\text{HARPS}}, a_{\text{PFS}}, \lambda_{\text{RV}}, \Gamma_{\text{RV}}, P_{\text{RV}}, s_{\text{TESS}}, s_{\text{HARPS}}, s_{\text{PFS}}, \gamma_{\text{TESS}}, \gamma_{\text{HARPS}}, \gamma_{\text{PFS}}, P_b, T_0, K, h, k, a/R_s, r_p/R_s, i, q_1, q_2\}.$

We sampled the posterior PDF of this 21-dimensional parameter space using an MCMC sampler. Details on the sampler and the adopted prior distributions on each model parameter are given in Appendix A and Table A.1.

5. Results

In our analysis of the light curve and radial velocity time series of L 168-9, we evaluated the model presented in Sect. 4.3 on the separate RV data sets obtained with HARPS and PFS as well as the combined time series. Subtracting the model to the 46 HARPS radial velocity points reduces the dispersion to 3.37 m s⁻¹ (equivalent to $\chi^2_{\rm red} = 3.5$), while the dispersion of the 76 PFS residual points gives 4.05 m s⁻¹ (translating into $\chi^2_{\rm red} = 1.5$). The dispersion obtained from the 122 HARPS+PFS residual points is 3.80 m s⁻¹ ($\chi^2_{\rm red} = 2.2$).

From point estimates of the model parameters Θ from our joint RV plus transit analysis with each of these input data sets, we confirm that L 168-9 b has a radius of $1.39 \pm 0.09 R_{\oplus}$ and a mass of $4.60 \pm 0.56 M_{\oplus}$, translating into a bulk mean density of $9.6^{+2.4}_{-1.8}$ g cm⁻³. The planet is orbiting at 0.02091 ± 0.00024 AU from the parent star; therefore, the hot terrestrial planet has an

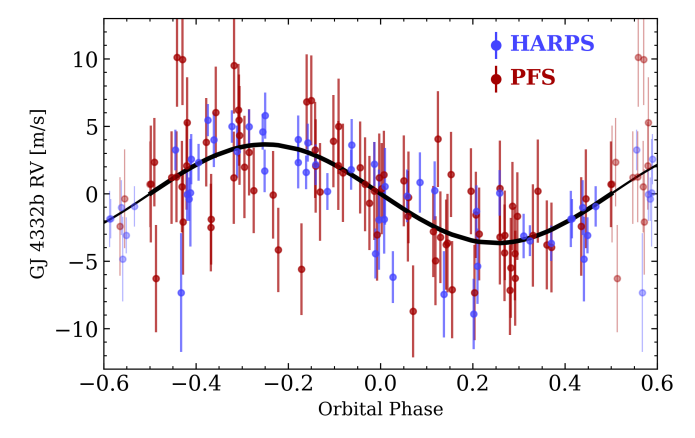


Fig. 7. Phase folded radial velocity acquired HARPS (blue points) and PFS (red points) where the best GP model was subtracted. The black curve represents the maximum a posteriori model adjusted to the data set.

equilibrium temperature between 668 and 965 K assuming a Venus-like and zero bond albedo, respectively. Results for the entire set of parameters are reported in Table 2. Explicitly, we report the maximum a posteriori value of each parameter along with its 16th and 84th percentiles, corresponding to a 1σ confidence interval. We checked for consistency in our joint analysis by performing the analysis for each instrument independently. Table 2 details the results from this test. We note that HARPS and PFS results are in agreement within their uncertainties, translating into a robust detection of the planetary signal in radial velocity data.

Figure 6 shows the TESS photometry and adjusted transit model and Fig. 7 illustrates the phase folded radial velocity with the model that best fits the data.

Table 3. Prospects of atmospheric characterization of confirmed terrestrial planets including L 168-9 b.

| Star ID units | $R_{ m p} \ [R_{\oplus}]$ | $M_{ m p}$ $[M_{\oplus}]$ | P [days] | a [AU] | T _{eff} [K] | <i>T</i> _{eq} [K] | T _{day} [K] | J [mag] | K _s [mag] | R_{\star} $[R_{\odot}]$ | M_{\star} $[M_{\odot}]$ | TSM | ESM | Ref. |
|---------------|---------------------------|---------------------------|-------------|-----------|----------------------|----------------------------|-------------------------|------------|----------------------|---------------------------|---------------------------|--------|--------|---------|
| L 168-9 b | 1.39 | 4.39 | 1.401 | 0.021 | 3743 | 963.01 | 1059.31 | 7.941 | 7.0819 | 0.60 | 0.62 | 8.025 | 9.692 | |
| LHS 3844 b | 1.30 | _ | 0.463 | 0.006 | 3036 | 805.90 | 886.49 | 10.046 | 9.145 | 0.19 | 0.15 | _ | 29.004 | Kr2019 |
| GJ 1132 b | 1.13 | 1.66 | 1.629 | 0.015 | 3270 | 590.61 | 649.67 | 9.245 | 8.322 | 0.21 | 0.18 | 31.166 | 9.872 | Bo2018 |
| L 98-59 c | 1.35 | 2.17 | 3.690 | 0.032 | 3412 | 515.31 | 566.84 | 7.933 | 7.101 | 0.31 | 0.31 | 29.168 | 6.696 | C12019b |
| LTT 1445A b | 1.38 | 2.20 | 5.359 | 0.038 | 3335 | 433.34 | 476.68 | 7.29 | 6.5 | 0.28 | 0.26 | 44.976 | 6.382 | Wi2019 |
| TRAPPIST-1 b | 1.09 | 1.02 | 1.511 | 0.011 | 2559 | 402.38 | 442.62 | 11.4 | 10.3 | 0.12 | 0.08 | 36.914 | 4.007 | Gi2017 |
| LHS 1140 c | 1.28 | 1.81 | 3.778 | 0.027 | 3216 | 436.43 | 480.07 | 9.612 | 8.821 | 0.21 | 0.18 | 25.225 | 3.401 | Me2019 |

Notes. TSM and ESM correspond to transmission and emission spectroscopy metrics, respectively.

References. Kr2019 – Kreidberg et al. (2019); Bo2018 – Bonfils et al. (2018); Cl2019b – Cloutier et al. (2019b); Wi2019 – Winters et al. (2019b); Gi2017 – Gillon et al. (2017); Me2019 – Ment et al. (2019).

6. Discussion and conclusions

L 168-9 b adds to the family of small ($<2\,R_\oplus$) transiting planets around bright (J<8 mag) stars with mass measurements and contributes to the completion of the TESS level one science requirement to detect and measure the masses of 50 small planets. In particular, L 168-9 b is one of fourteen⁹ likely rocky planets without primordial hydrogen-helium envelopes – that is, it has a radius $<1.8\,R_\oplus$ – for which the mass has been measured with an uncertainty that is smaller than 33%. Thus, our result represents progress toward the understanding of the transition between super-Earths and mini-Neptunes as previously reported in the radii of planets (e.g., Fulton et al. 2017; Cloutier & Menou 2019) but, here, it includes information about mass.

Figure 8 shows the mass-radius diagram that is centered in the sub-Earth to mini-Neptune regime. With about twice the Earth average density, L 168-9 b bulk density is compatible with a terrestrial planet with an iron core (50%) surrounded by a mantle of silicates (50%). In this diagram the detected planet is located in an interesting place: for masses lower than that of L 168-9 b, the great majority of planets are consistent with a 50% Fe–50% MgSiO3 or 100% MgSiO3 bulk composition, while there is a great diversity in density for higher planetary masses. Being one of the densest planets for masses greater than $4 M_{\oplus}$, L 168-9 b can help to define the mass limits of the rocky planets population.

Good targets for atmospheric characterization with transmission and emission spectroscopy are those transiting nearby, bright stars (J < 8 mag). There are currently 11 small planets detected transiting a bright star, according to the NASA Exoplanet Archive¹⁰, two of them orbit M dwarfs. Overall, there would not be a large number of small, transiting planets around nearby, bright M dwarfs. There are roughly 200 M dwarfs within the 25 pc solar neighborhood with J < 8 mag, about 2/3 of which are single stars (Winters et al. 2015, 2019a). Considering the occurrence rate of small planets with an orbital period that is

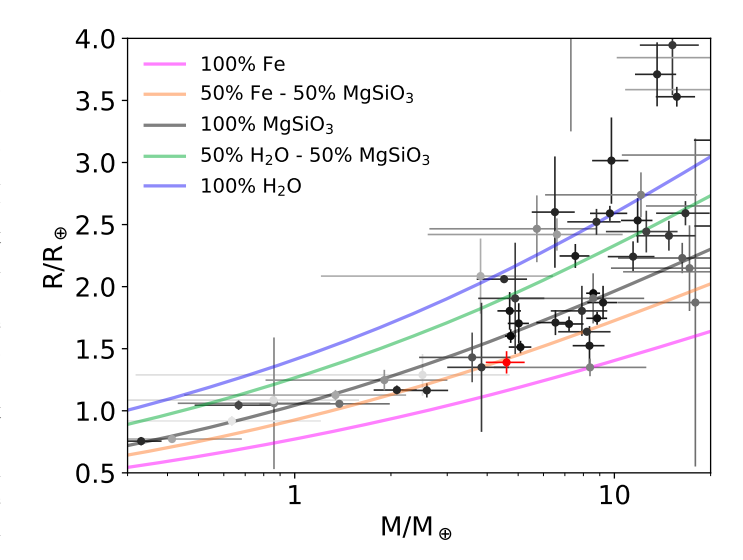


Fig. 8. Mass-radius diagram showing L 168-9 b (red circle) in the context of known exoplanets. The transparency of each point is proportional to its associated mass uncertainty. Error bars correspond to 1σ uncertainties. Different models for the bulk composition are plotted where the legend details the fraction of iron, silicates, and/or water for each color-coded curve.

shorter than 10 days from Dressing & Charbonneau (2015) and combining this with the transit probability of such planets (about a couple % to \sim 20%), there would be a few and up to about twenty such planets.

The measured properties of L 168-9 b and its host star make it a promising target for the atmospheric characterization of a terrestrial planet via either transmission or emission spectroscopy measurements with JWST (Morley et al. 2017; Kempton et al. 2018) and/or thermal phase curve analysis to infer the absence of a thick atmosphere (e.g., Seager & Deming 2009). Its transmission and emission spectroscopy metrics from Kempton et al. (2018) are reported in Table 3 and they are compared to other confirmed transiting terrestrial planets with known masses that are of interest for atmospheric characterization. Based on this assessment, L 168-9 b is an excellent candidate for emission spectroscopy or for detecting the planetary day-side phase curve as was recently done for the similar planet, LHS 3844 b (Kreidberg et al. 2019).

⁹ L 98-59 bc (Cloutier et al. 2019b), GJ 357 b (Luque et al. 2019), HD 15337 b (Dumusque et al. 2019), HD 213885 b (Espinoza et al. 2020), GJ 9827 b (Rice et al. 2019), K2-265 b (Lam et al. 2018), K2-141 b (Barragán et al. 2018), K2-229 b (Santerne et al. 2018), HD 3167 b (Gandolfi et al. 2017), K2-106 b (Guenther, E. W. et al. 2017), TRAPPIST-1 fh (Wang et al. 2017), HD 219134 b (Motalebi et al. 2015). ¹⁰ https://exoplanetarchive.ipac.caltech.edu/

Acknowledgements. N.A.-D. acknowledges the support of FONDECYT project 3180063. J.K.T. acknowledges that support for this work was provided by NASA through Hubble Fellowship grant HST-HF2-51399.001 awarded by the Space Telescope Science Institute, which is operated by the Association of Universities for Research in Astronomy, Inc., for NASA, under contract NAS5-26555. R.B. acknowledges support from FONDECYT Post-doctoral Fellowship Project 3180246, and from the Millennium Institute of Astrophysics (MAS). X.B. and J.M-A. acknowledge funding from the European Research Council under the ERC Grant Agreement n. 337591-ExTrA. X.D., X.B., T.F., and L.M. acknowledge the support by the French National Research Agency in the framework of the Investissements d'Avenir program (ANR-15-IDEX-02), through the funding of the "Origin of Life" project of the Univ. Grenoble-Alpes. L.M. acknowedges the support of the Labex OSUG@2020 (Investissements d'avenir – ANR10 LABX56). J.R.M. acknowledges CAPES, CNPq and FAPERN brazilian agencies. This work was supported by FCT/MCTES through national funds and by FEDER - Fundo Europeu de Desenvolvimento Regional through COM-PETE2020 - Programa Operacional Competitividade e Internacionalização by these grants: UID/FIS/04434/2019; PTDC/FIS-AST/32113/2017 & POCI-01-0145-FEDER-032113; PTDC/FIS-AST/28953/2017 & POCI-01-0145-FEDER-028953. T.H. acknowledges support from the European Research Council under the Horizon 2020 Framework Program via the ERC Advanced Grant Origins 83 24 28. R.E.M. acknowledges support by the BASAL Centro de Astrofísica y Tecnologías Afines (CATA) and FONDECYT 1190621. A.J. acknowledges support from FONDECYT project 1171208 and by the Ministry for the Economy, Development, and Tourism's Programa Iniciativa Científica Milenio through grant IC 120009, awarded to the Millennium Institute of Astrophysics (MAS). J.G.W. is supported by a grant from the John Templeton Foundation. The opinions expressed here are those of the authors and do not necessarily reflect the views of the John Templeton Foundation. Work of J.N.W. was partly funded by the Heising-Simons Foundation. The authors would like to acknowledge Zachary Hartman for his help conducting the Gemini-South/DSSI observations. Some of the work here is based on observations obtained at the Gemini Observatory, which is operated by the Association of Universities for Research in Astronomy, Inc., under a cooperative agreement with the NSF on behalf of the Gemini partnership: the National Science Foundation (United States), National Research Council (Canada), CONICYT (Chile), Ministerio de Ciencia, Tecnología e Innovación Productiva (Argentina), Ministério da Ciência, Tecnologia e Inovação (Brazil), and Korea Astronomy and Space Science Institute (Republic of Korea). This work makes use of observations from the LCOGT network. Funding for the TESS mission is provided by NASA's Science Mission directorate. We acknowledge the use of public TESS Alert data from pipelines at the TESS Science Office and at the TESS Science Processing Operations Center. This research has made use of the Exoplanet Follow-up Observation Program website, which is operated by the California Institute of Technology, under contract with the National Aeronautics and Space Administration under the Exoplanet Exploration Program. Resources supporting this work were provided by the NASA High-End Computing (HEC) Program through the NASA Advanced Supercomputing (NAS) Division at Ames Research Center for the production of the SPOC data products. This paper includes data collected by the TESS mission, which are publicly available from the Mikulski Archive for Space Telescopes (MAST). This research has made use of the NASA Exoplanet Archive, which is operated by the California Institute of Technology, under contract with the National Aeronautics and Space Administration under the Exoplanet Exploration Program.

References

```
Allard, F. 2014, IAU Symp., 299, 271
Anglada-Escudé, G., & Butler, R. P. 2012, ApJS, 200, 15
Angus, R., Morton, T., Aigrain, S., Foreman-Mackey, D., & Rajpaul, V. 2018,
   MNRAS, 474, 2094
Astudillo-Defru, N., Delfosse, X., Bonfils, X., et al. 2017a, A&A, 600, A13
Astudillo-Defru, N., Forveille, T., Bonfils, X., et al. 2017b, A&A, 602, A88
Astudillo-Defru, N., Díaz, R. F., Bonfils, X., et al. 2017c, A&A, 605, L11
Baranne, A., Queloz, D., Mayor, M., et al. 1996, A&AS, 119, 373
Barragán, O., Gandolfi, D., Dai, F., et al. 2018, A&A, 612, A95
Batalha, N. E., Lewis, T., Fortney, J. J., et al. 2019, ApJ, 885, L25
Bayo, A., Rodrigo, C., Barrado Y Navascués, D., et al. 2008, A&A, 492, 277
Beichman, C. A., Bryden, G., Stapelfeldt, K. R., et al. 2006, ApJ, 652, 1674
Bonfils, X., Almenara, J.-M., Cloutier, R., et al. 2018, A&A, 618, A142
Brown, T. M., Baliber, N., Bianco, F. B., et al. 2013, PASP, 125, 1031
Butler, R. P., Marcy, G. W., Williams, E., et al. 1996, PASP, 108, 500
Charbonneau, D., Brown, T. M., Latham, D. W., & Mayor, M. 2000, ApJ, 529,
  L45
Ciardi, D. R., Beichman, C. A., Horch, E. P., & Howell, S. B. 2015, ApJ, 805, 16
```

Cloutier, R., & Menou, K. 2019, AAS J., submitted [arXiv:1912.02170]

Cloutier, R., Astudillo-Defru, N., Doyon, R., et al. 2017, A&A, 608, A35 Cloutier, R., Astudillo-Defru, N., Doyon, R., et al. 2019a, A&A, 621, A49

```
Collins, K. A., Kielkopf, J. F., Stassun, K. G., & Hessman, F. V. 2017, AJ, 153,
Crane, J. D., Shectman, S. A., & Butler, R. P. 2006, Proc. SPIE, 6269, 626931
Crane, J. D., Shectman, S. A., Butler, R. P., Thompson, I. B., & Burley, G. S.
   2008, Proc. SPIE, 7014, 701479
Crane, J. D., Shectman, S. A., Butler, R. P., et al. 2010, Proc. SPIE, 7735, 773553
Cutri, R. M., Skrutskie, M. F., van Dyk, S., et al. 2003, VizieR Online Data
  Catalog: II/246
Cutri, R. M., Wright, E. L., Conrow, T., et al. 2013, VizieR Online Data Catalog:
   II/328
de Zeeuw, T., Tamai, R., & Liske, J. 2014, The Messenger, 158, 3
Dressing, C. D., & Charbonneau, D. 2015, ApJ, 807, 45
Dumusque, X., Turner, O., Dorn, C., et al. 2019, A&A, 627, A43
Espinoza, N., Brahm, R., Henning, T., et al. 2020, MNRAS, 491, 2982
Faria, J. P., Haywood, R. D., Brewer, B. J., et al. 2016, A&A, 588, A31
Foreman-Mackey, D., Hogg, D. W., Lang, D., & Goodman, J. 2013, PASP, 125,
Fulton, B. J., Petigura, E. A., Howard, A. W., et al. 2017, AJ, 154, 109
Gaia Collaboration 2018, VizieR Online Data Catalog: I/345
Gaidos, E., Mann, A. W., Lépine, S., et al. 2014, MNRAS, 443, 2561
Gandolfi, D., Barragán, O., Hatzes, A. P., et al. 2017, AJ, 154, 123
Gardner, J. P., Mather, J. C., Clampin, M., et al. 2006, Space Sci. Rev., 123, 485
Giles, H. A. C., Collier Cameron, A., & Haywood, R. D. 2017, MNRAS, 472,
   1618
Gillon, M., Triaud, A. H. M. J., Demory, B.-O., et al. 2017, Nature, 542, 456
Goodman, J., & Weare, J. 2010, Commun. Appl. Math. Comput. Sci., 5, 65
Grunblatt, S. K., Howard, A. W., & Haywood, R. D. 2015, ApJ, 808, 127
Guenther, E. W., Barragán, O., Dai, F., et al. 2017, A&A, 608, A93
Hauschildt, P. H., Allard, F., & Baron, E. 1999, ApJ, 512, 377
Haywood, R. D., Collier Cameron, A., Queloz, D., et al. 2014, MNRAS, 443,
Henden, A. A., Templeton, M., Terrell, D., et al. 2016, VizieR Online Data
  Catalog: II/336
Henry, G. W., Marcy, G. W., Butler, R. P., & Vogt, S. S. 2000, ApJ, 529, L41
Høg, E., Fabricius, C., Makarov, V. V., et al. 2000, A&A, 355, L27
Horch, E. P., Veillette, D. R., Baena Gallé, R., et al. 2009, AJ, 137, 5057
Horch, E. P., Gomez, S. C., Sherry, W. H., et al. 2011, AJ, 141, 45
Horch, E. P., Howell, S. B., Everett, M. E., & Ciardi, D. R. 2012, AJ, 144, 165
Howell, S. B., Everett, M. E., Sherry, W., Horch, E., & Ciardi, D. R. 2011, AJ,
   142, 19
Jenkins, J. M., Twicken, J. D., McCauliff, S., et al. 2016, SPIE Conf. Ser., 9913,
   99133E
Jensen, E. 2013, Astrophysics Source Code Library [ascl:1306.007]
Kempton, E. M.-R., Bean, J. L., Louie, D. R., et al. 2018, PASP, 130, 114401
Kipping, D. M. 2013, MNRAS, 435, 2152
Kreidberg, L., Koll, D. D. B., Morley, C., et al. 2019, Nature, 573, 87
Lam, K. W. F., Santerne, A., Sousa, S. G., et al. 2018, A&A, 620, A77
Lo Curto, G., Pepe, F., Avila, G., et al. 2015, The Messenger, 162, 9
López-Morales, M., Haywood, R. D., Coughlin, J. L., et al. 2016, AJ, 152, 204
Lovis, C., & Pepe, F. 2007, A&A, 468, 1115
Luque, R., Pallé, E., Kossakowski, D., et al. 2019, A&A, 628, A39
Mandel, K., & Agol, E. 2002, ApJ, 580, L171
Mann, A. W., Dupuy, T., Kraus, A. L., et al. 2019, ApJ, 871, 63
Mayor, M., Pepe, F., Queloz, D., et al. 2003, The Messenger, 114, 20
Mazeh, T., Naef, D., Torres, G., et al. 2000, ApJ, 532, L55
Ment, K., Dittmann, J. A., Astudillo-Defru, N., et al. 2019, AJ, 157, 32
Moór, A., Ábrahám, P., Derekas, A., et al. 2006, ApJ, 644, 525
Morley, C. V., Kreidberg, L., Rustamkulov, Z., Robinson, T., & Fortney, J. J.
  2017, ApJ, 850, 121
Mortier, A., Faria, J. P., Santos, N. C., et al. 2016, A&A, 585, A135
Motalebi, F., Udry, S., Gillon, M., et al. 2015, A&A, 584, A72
Muirhead, P. S., Dressing, C. D., Mann, A. W., et al. 2018, AJ, 155, 180
Neves, V., Bonfils, X., Santos, N. C., et al. 2014, A&A, 568, A121
Pollacco, D. L., Skillen, I., Collier Cameron, A., et al. 2006, PASP, 118, 1407
Queloz, D., Henry, G. W., Sivan, J. P., et al. 2001, A&A, 379, 279
Rice, K., Malavolta, L., Mayo, A., et al. 2019, MNRAS, 484, 3731
Ricker, G. R., Winn, J. N., Vanderspek, R., et al. 2015, J. Astron. Telesc. Instrum.
   Syst., 1, 014003
Santerne, A., Brugger, B., Armstrong, D. J., et al. 2018, Nat. Astron., 2, 393
Seager, S., & Deming, D. 2009, ApJ, 703, 1884
Smith, J. C., Stumpe, M. C., Van Cleve, J. E., et al. 2012, PASP, 124, 1000
Stassun, K. G., & Torres, G. 2016, AJ, 152, 180
Stassun, K. G., & Torres, G. 2018, ApJ, 862, 61
Stassun, K. G., Collins, K. A., & Gaudi, B. S. 2017, AJ, 153, 136
Stassun, K. G., Corsaro, E., Pepper, J. A., & Gaudi, B. S. 2018a, AJ, 155, 22
Stassun, K. G., Oelkers, R. J., Pepper, J., et al. 2018b, AJ, 156, 102
Stumpe, M. C., Smith, J. C., Catanzarite, J. H., et al. 2014, PASP, 126, 100
```

Cloutier, R., Astudillo-Defru, N., Bonfils, X., et al. 2019b, A&A, 629, A111

Sullivan, P. W., Winn, J. N., Berta-Thompson, Z. K., et al. 2015, ApJ, 809, 77 Teske, J. K., Shectman, S. A., Vogt, S. S., et al. 2016, AJ, 152, 167

Teske, J. K., Ciardi, D. R., Howell, S. B., Hirsch, L. A., & Johnson, R. A. 2018, AJ, 156, 292

Tokovinin, A. 2018, PASP, 130, 035002

Twicken, J. D., Catanzarite, J. H., Clarke, B. D., et al. 2018, PASP, 130, 064502Wang, S., Wu, D.-H., Barclay, T., & Laughlin, G. P. 2017, ApJ, submitted [arXiv:1704.04290]

Winters, J. G., Henry, T. J., Lurie, J. C., et al. 2015, AJ, 149, 5 Winters, J. G., Henry, T. J., Jao, W.-C., et al. 2019a, AJ, 157, 216 Winters, J. G., Medina, A. A., Irwin, J. M., et al. 2019b, AJ, 158, 152 Zechmeister, M., & Kürster, M. 2009, A&A, 496, 577 Ziegler, C., Law, N. M., Baranec, C., et al. 2018, AJ, 155, 161 Ziegler, C., Tokovinin, A., Briceno, C., et al. 2020, AJ, 159, 19

- Departamento de Matemática y Física Aplicadas, Universidad Católica de la Santísima Concepción, Alonso de Rivera 2850, Concepción, Chile
 - e-mail: nastudillo@ucsc.cl
- ² Center for Astrophysics | Harvard & Smithsonian, 60 Garden Street, Cambridge, MA 02138, USA
- Department of Astronomy & Astrophysics, University of Toronto, 50 St. George Street, Toronto, ON, M5S 3H4, Canada
- Observatories of the Carnegie Institution for Science, 813 Santa Barbara Street, Pasadena, CA 91101, USA
- ⁵ Center of Astro-Engineering UC, Pontificia Universidad Católica de Chile, Av. Vicuña Mackenna 4860, 7820436 Macul, Santiago, Chile
- ⁶ Instituto de Astrofísica, Facultad de Física, Pontificia Universidad Católica de Chile, Av. Vicuña Mackenna 4860, 7820436 Macul, Santiago, Chile
- ⁷ Millennium Institute of Astrophysics, Santiago, Chile
- ⁸ Astrophysics Group, Keele University, Staffordshire, ST5 5BG, UK
- ⁹ Kavli Institute for Astrophysics and Space Research, Massachusetts Institute of Technology, Cambridge, MA 02139, USA
- Department of Earth, Atmospheric, and Planetary Sciences, Massachusetts Institute of Technology, Cambridge, MA 02139, USA
- Department of Astrophysical Sciences, Princeton University, Princeton, NJ 08544, USA
- NASA Ames Research Center, Moffett Field, CA 94035, USA
- Department of Physics and Astronomy, Vanderbilt University, Nashville, TN 37235, USA
- ¹⁴ Dunlap Institute for Astronomy and Astrophysics, University of Toronto, Ontario M5S 3H4, Canada
- ¹⁵ Univ. Grenoble Alpes, CNRS, IPAG, 38000 Grenoble, France
- ¹⁶ Department of Physics, University of Warwick, Gibbet Hill Road, Coventry CV4 7AL, UK
- ¹⁷ Institut de Recherche sur les Exoplanètes, Département de Physique, Université de Montréal, Montréal QC, H3C 3J7, Canada
- ¹⁸ Observatoire de Genève, Université de Genève, 51 ch. des Maillettes, 1290 Sauverny, Switzerland

- ¹⁹ Cerro Tololo Inter-American Observatory, Casilla 603, La Serena, Chile
- Department of Terrestrial Magnetism, Carnegie Institution for Science, 5241 Broad Branch Road NW, Washington DC 20015, USA
- American Association of Variable Star Observers, 49 Bay State Road, Cambridge, MA 02138, USA
- Department of Physics, and Kavli Institute for Astrophysics and Space Research, Massachusetts Institute of Technology, Cambridge, MA, USA
- ²³ Physics & Astronomy Department, University of Kansas, Lawrence, KS 66044, USA
- ²⁴ Universidad de Buenos Aires, Facultad de Ciencias Exactas y Naturales. Buenos Aires, Argentina
- ²⁵ CONICET Universidad de Buenos Aires, Instituto de Astronomía y Física del Espacio (IAFE), Buenos Aires, Argentina
- ²⁶ Department of Physics and Astronomy, University of New Mexico, Albuquerque, NM, USA
- ²⁷ Space Telescope Science Institute, 3700 San Martin Drive, Baltimore, MD 21218, USA
- ²⁸ European Southern Observatory, Alonso de Córdova 3107, Vitacura, Región Metropolitana, Chile
- ²⁹ Universidad de Concepción, Departamento de Astronomía, Casilla 160-C, Concepción, Chile
- ³⁰ Physics Department and Tsinghua Centre for Astrophysics, Tsinghua University, Beijing 100084, PR China
- 31 Centre for Astrophysics, University of Southern Queensland, Toowoomba, QLD 4350, Australia
- Max-Planck-Institut fur Astronomie, Künigstuhl 17, 69117 Heidelberg, Germany
- ³³ Department of Physics, Southern Connecticut State University, 501 Crescent Street, New Haven, CT 06515, USA
- 34 Campo Catino Astronomical Observatory, Regione Lazio, Guarcino (FR) 03010, Italy
- ³⁵ Departamento de Astronomía, Universidad de Chile, Camino El Observatorio 1515, Las Condes, Santiago, Chile
- ³⁶ Facultad de Ingeniería y Ciencias, Universidad Adolfo Ibáñez, Av. Diagonal las Torres 2640, Peñalolén, Santiago, Chile
- ³⁷ Department of Physics and Astronomy, University of Louisville, Louisville, KY 40292, USA
- ³⁸ Department of Physics and Astronomy, The University of North Carolina at Chapel Hill, Chapel Hill, NC 27599-3255, USA
- ³⁹ Departamento de Física, Universidade Federal do Rio Grande do Norte, 59078-970 Natal, RN, Brazil
- ⁴⁰ Georgia State University, Department of Physics & Astronomy, 25 Park Place NE #605, USA
- ⁴¹ Instituto de Astrofísica e Ciências do Espaço, Universidade do Porto, CAUP, Rua das Estrelas, PT4150-762 Porto, Portugal
- ⁴² Departamento de Física e Astronomia, Faculdade de Ciências, Universidade do Porto, Porto, Portugal
- ⁴³ SETI Institute, Moffett Field, CA 94035, USA
- ⁴⁴ Center for Space Research, MIT, 37-414, Cambridge, MA 02139, USA

Appendix A: Gaussian process model

Gaussian process (GP) regression is widely used in the exoplanet community as a nonparametric Bayesian approach to model temporally correlated stellar activity signals in RV data. These rotationally-modulated activity signals prohibit the accurate measurement of planetary parameters and often produce in planetary false positives.

Here, we modeled the RV activity signals of L 168-9 as a stochastic process whose temporal evolution is well-described by a quasi-periodic covariance kernel. A GP with a quasi-periodic covariance kernel $k(t_i, t_j)$ is included in our joint model describing the data RV and transit data and takes the following form:

$$k(t_i, t_j) = a^2 \exp\left[-\frac{(t_i - t_j)^2}{2\lambda^2} - \Gamma^2 \sin^2\left(\frac{\pi |t_i - t_j|}{P_{GP}}\right)\right]$$
(A.1)

and is described by the covariance amplitude a, the exponential evolutionary timescale λ , the coherence Γ , and the periodic timescale P_{GP} .

As usual in the Bayesian context, prior probability density functions (PDF) for the hyperparameters $\{a, \lambda, \Gamma, P_{GP}\}$ are listed in Table A.1 for the multiple GPs that were applied in our data analysis. The posterior PDF were sampled through a MCMC (Goodman & Weare 2010); in particular, we used the emcee ensemble sampler (Foreman-Mackey et al. 2013). The sampling of the joint posterior was made with the Gaussian ln likelihood function given by

$$\ln \mathcal{L} = -\frac{1}{2} \left(y^{\mathrm{T}} \cdot K \cdot y + \ln \det K + N \ln 2\pi \right) \tag{A.2}$$

where y is the vector of N measurements taken at times $t = \{t_1, t_2, \dots, t_N\}$ and the $N \times N$ covariance matrix K is given by

$$K_{ij} = k(t_i, t_j) + \delta_{ij} [\sigma(t_i)^2 + s^2]$$
 (A.3)

Table A.1. L 168-9 model parameter priors.

| Parameter | Prior |
|---|----------------------------|
| Photometry model | |
| Baseline flux, γ_{TESS} | $\mathcal{U}(-0.1, 0.1)$ |
| Limb darkening coefficient, u_1 | U(0.1, 0.4) |
| Limb darkening coefficient, u_2 | $\mathcal{U}(0.25, 0.55)$ |
| TESS additive jitter, s_{TESS} | $\mathcal{J}(10^{-2},1)$ |
| RV model | |
| HARPS zero point velocity, $\gamma_{0,HARPS}$ [m s ⁻¹] | U(-1,1) |
| PFS zero point velocity, $\gamma_{0,PFS}$ [m s ⁻¹] | U(-1,1) |
| ln HARPS covariance amplitude, $\ln (a_{\text{HARPS}}/\text{m s}^{-1})$ | U(-5, 10) |
| ln PFS covariance amplitude, $\ln (a_{PFS}/\text{m s}^{-1})$ | U(-5, 10) |
| ln RV exponential time scale, $\ln (\lambda_{RV}/\text{day})$ | From H α training |
| $\ln RV$ coherence, $\ln (\Gamma_{RV})$ | From H α training |
| $\ln RV$ periodic timescale, $\ln (P_{RV}/\text{day})$ | From H α training |
| HARPS additive jitter, s_{HARPS} [m s ⁻¹] | $\mathcal{J}(10^{-2}, 10)$ |
| PFS additive jitter, s_{PFS} [m s ⁻¹] | $\mathcal{J}(10^{-2}, 10)$ |
| L 168-9 b (TOI-134.01) | |
| Orbital period, P_b [days] | U(1.370, 1.405) |
| Time of midtransit, $T_{0,b}$ [BJD – 2457 000] | U(338, 1342) |
| Scaled semimajor axis, a/R_s | G(7.542, 0.27) |
| Planet-star radius ratio, r_p/R_s | U(0, 0.1) |
| Orbital inclination, <i>i</i> [deg] | U(75, 105) |
| Semiamplitude, K_b [m s ⁻¹] | $\mathcal{J}(10^{-2}, 10)$ |
| $h_b = \sqrt{e_b} \cos \omega_b$ | U(-1,1) |
| $k_b = \sqrt{e_b} \sin \omega_b$ | $\mathcal{U}(-1,1)$ |

with δ_{ij} being the Kronecker delta that adds the measurement uncertainties σ to the diagonal elements of K and includes an additive jitter factor s.

Appendix B: Spectroscopic data

Table B.1. HARPS radial velocity time series and spectroscopic activity indicators for L 168-9.

| BJD [-2 450 000] | RV [ms ⁻¹] | $\sigma_{ m RV}$ [ms ⁻¹] | $\mathrm{H}lpha$ | $\sigma_{ m Hlpha}$ | $H\beta$ | $\sigma_{	ext{H}eta}$ | Нγ | $\sigma_{ m H\gamma}$ | NaD | $\sigma_{ m NaD}$ | S | σ_{S} |
|---------------------|---------------------------|--------------------------------------|------------------|---------------------|----------|-----------------------|---------|-----------------------|---------|-------------------|-------|--------------|
| 4664.954608 | 29 781.65 | 3.48 | 0.06224 | 0.00025 | 0.04679 | 0.00052 | 0.10087 | 0.00131 | 0.01232 | 0.00020 | 1.616 | 0.068 |
| 4991.927461 | 29 786.04 | 2.95 | 0.06074 | 0.00021 | 0.04632 | 0.00044 | 0.10385 | 0.00114 | 0.01172 | 0.00016 | 2.167 | 0.073 |
| 8367.523380 | 29 769.97 | 1.37 | 0.05962 | 0.00011 | 0.04606 | 0.00019 | 0.10582 | 0.00052 | 0.01166 | 0.00007 | 1.892 | 0.018 |
| 8367.551447 | 29 773.09 | 1.19 | 0.05928 | 0.00010 | 0.04534 | 0.00016 | 0.10573 | 0.00045 | 0.01158 | 0.00006 | 1.826 | 0.014 |
| 8367.623921 | 29 772.57 | 1.20 | 0.05944 | 0.00010 | 0.04562 | 0.00017 | 0.10639 | 0.00046 | 0.01164 | 0.00006 | 1.868 | 0.014 |

Notes. The full version is available at the CDS.

Table B.2. PFS radial velocity time series and spectroscopic activity indicators.

| BJD | RV | σ_{RV} | Нα | S |
|------------|-------------|---------------|-------|---------|
| [-2450000] | $[ms^{-1}]$ | $[ms^{-1}]$ | | |
| 8409.51799 | 8.80 | 1.74 | 1.293 | 0.05807 |
| 8409.53206 | 4.10 | 1.74 | 1.334 | 0.05813 |
| 8409.60491 | -3.11 | 1.71 | 1.285 | 0.05879 |
| 8409.61960 | 4.80 | 1.75 | 1.340 | 0.05901 |
| 8409.67495 | 8.23 | 2.09 | 1.311 | 0.05976 |

Notes. The full version is available at the CDS.